Enhanced wide-angle third-harmonic generation in flat-band-engineered quasi-BIC metagratings

Yijia Zang[1], Ruoheng Chai[1], Wenwei Liu[1*], Zhancheng Li[1], Hua Cheng[1*], Jianguo Tian[1], and Shuqi Chen[1,2,3*]

[1] *The Key Laboratory of Weak Light Nonlinear Photonics, Ministry of Education, School of Physics and TEDA Institute of Applied Physics, Nankai University, Tianjin 300071, China;*
[2] *School of Materials Science and Engineering, Smart Sensing Interdisciplinary Science Center, Nankai University, Tianjin 300350, China;*
[3] *The Collaborative Innovation Center of Extreme Optics, Shanxi University, Taiyuan 030006, China*

Nonlinear metasurfaces and photonic crystals provide a significant way to generate and manipulate nonlinear signals owing to the resonance- and symmetry-based light-matter interactions supported by the artificial structures. However, the nonlinear conversion efficiency is generally limited by the angular dispersion of optical resonances especially in nonparaxial photonics. Here, we propose a metagrating realizing a quasi-bound-state in the continuum in a flat band to dramatically improve the third harmonic generation (THG) efficiency. A superior operating angular range is achieved based on the interlayer and intralayer couplings, which are introduced by breaking the mirror symmetry of the metagrating. We demonstrate the relation of angular dispersion between the nonlinear and linear responses at different incident angles. We also elucidate the mechanism of these off-axis flat-band-based nonlinear conversions through different mode decomposition. Our scheme provides a robust and analytical way for nonparaxial nonlinear generation and paves the way for further applications such as wide-angle nonlinear information transmission and enhanced nonlinear generation under tight focusing.

nonlinear metasurfaces, quasi-bound-state in the continuum, angular dispersion, third harmonic generation efficiency

PACS number(s): 42.79.Dj, 42.65.-k, 63.20.Pw, 42.65.Ky, 42.65.Wi

1 Introduction

Nonlinear optics studies the results of the modified optical properties when intense light passes through an optical medium, such as two-photon absorption [1,2], four-wave mixing [3,4], and harmonics generation [5-7]. Conventional nonlinear generation enhancement is nonresonant and achieved by increasing the distance of light-matter interac-

tion with strict phase-matching conditions [8,9], which inevitably leads to bulky devices. With the advantage of strong resonant local-field enhancements and flexible manipulation of harmonic waves, subwavelength metasurfaces [10-14] can drastically improve the nonlinear conversion efficiency with significantly relaxed phase-matching requirements. Recently, all-dielectric metasurfaces harnessing Mie resonances have attracted much attention because of their large local enhancement, convenient fabrication, and low intrinsic losses. In addition, based on the concept of bound states in the continuum (BICs) [15], radiative Q factors can be engineered

---

*Corresponding authors (Wenwei Liu, email: wliu@nankai.edu.cn; Hua Cheng, email: hcheng@nankai.edu.cn; Shuqi Chen, email: schen@nankai.edu.cn)

to infinity to further improve the local-field enhancements and nonlinear conversion efficiency. To effectively excite the BIC mode in free space, BICs are usually transformed into quasi-BICs [16-18], which have controllable interactions with the radiative continuum. Recent studies have demonstrated applications of quasi-BICs in efficient nonlinear processes, such as harmonic generation [19,20], lasing [21-23], and optical frequency mixing [24-26].

Based on the energy band dispersion, different k components of the nonparaxial incidence will cause shifts in the resonant frequencies, leading to angular dispersion [27]. To address this issue, researchers have developed various approaches to eliminate the angular dispersion in the linear regime, such as engineering a flat band in momentum space [28-30], designing local optical responses for each incident angle in real space [31], or exploiting nonlocal modes to collectively modify the scattering characteristics [32]. Nevertheless, the nonlinear conversion efficiency is still limited due to angular dispersion. Recently, Huang et al. [28] theoretically proposed a moiré quasi-BIC flat band through interlayer coupling and opened up the possibility of improving the second-harmonic generation (SHG) efficiency with angle-limited nonparaxial wave excitation. However, there are still some issues that need to be clarified in the nonlinear regime: for example, can a structure with weak angular dispersion also generate a nonlinear signal with similar dispersion? The mechanism of the off-axis nonlinearity also needs to be further elucidated, and the superposition of harmonic signals excited by plane-wave components with different angles is also ambiguous.

In this work, we obtain a quasi-BIC flat band by interlayer and intralayer diffractive coupling in a quasi-BIC metagrating with broken mirror symmetry. We show that the angular dispersion of the nonlinear output signal cannot be directly obtained by that of the linear regime under plane-wave incidence with different angles. The mechanism of these off-axis flat-band-based nonlinear conversions is analyzed through different mode decompositions. The enhanced nonlinear conversion efficiency is realized by spectral overlap and constructive superposition. Compared with the dispersive-band-based nonlinear conversion efficiency, the flat-band-based higher counterpart is robust under normal and large-numerical-aperture (NA) oblique incidence. These results promote research on angular dispersion in the nonlinear regime and can easily provide extended applications involving different wide-angle components in informational photonic systems.

2 Design of the quasi-BIC flat band

We start with flat-band engineering exploiting a double-layer "*fishbone*" metagrating that consists of a sawtooth grating

and a comb waveguide grating, as shown in Figure 1(a) and (b), with the imaginary dotted line facilitating modeling and theoretical analysis. Our doublet fishbone structure may be fabricated using the e-beam lithography method of all-dielectric metasurface doublet (MD), which is developed and implemented by vertically concatenating two arrays of nanoresonators on either side of the substrate, as reported in ref. [33]. The layer misalignment is denoted as Sa, where $2a$ is the period and S is the dimensionless layer misalignment. In general, the energy band in such resonant gratings is dispersive (Figure 1(c)), leading to a low nonlinear conversion efficiency under wide-angle incidence. By tuning the diffraction phase shift $e^{\pm i\varphi}$ with $\varphi = 2\pi S$, which is essential for the dispersive evolution of energy bands (Supporting Material I), a flat band is generated, as depicted in Figure 1(d). To describe the physical mechanism of flat band generation, we introduce an analytical Hamiltonian model [29] corresponding to the "*fishbone*" metagratings. Based on the forward (a_{1+}, a_{2+}) and backward (a_{1-}, a_{2-}) fundamental zero-order waveguide modes of the double-layer gratings (Figure 1(a)), the 4×4 Hamiltonian H is given by

$$H=$$

$$\begin{pmatrix} \omega_1 + v_1 k_x & U_1 + \kappa_1 U_2 e^{i\varphi} & V & 0 \\ U_1 + \kappa_1 U_2 e^{-i\varphi} & \omega_1 - v_1 k_x & 0 & V \\ V & 0 & \omega_2 - v_2 k_x & U_2 e^{i\varphi} + \kappa_2 U_1 \\ 0 & V & U_2 e^{-i\varphi} + \kappa_2 U_1 & \omega_2 - v_2 k_x \end{pmatrix}.$$

$$(1)$$

We consider the first-order diffractive coupling processes between forward and backward waveguide modes since they are the most effective terms in the vicinity of the second-order Γ point [34,35]. $U_{1,2}$ are the intralayer diffractive coupling rates between the forward and backward waves in each layer. V represents the interlayer coupling between waves of the two gratings in the same direction. The factors $\kappa_{1,2}$ are indirect diffractive couplings between the evanescent fields of one grating and the waveguide modes of the other grating. The coefficient $e^{\pm i\varphi}$ ($\varphi = 2\pi S$) represents the first-order diffraction phase shift resulting from the layer misalignment Sa. $\omega_{1,2}$ and $v_{1,2}$ are the energies and group velocities of propagating guided waves. The detailed derivation of the eigenvalue problem is provided in the supplementary material (Supporting Material I). Since the first-order diffraction phase shift at $k_x = 0$ should meet the flat-band condition $d^n\omega / dk_x^n = 0 (n \geqslant 1, n \in Z)$, we obtain

$$\cos\varphi = \frac{2V^2}{U_1 U_2} - 1. \qquad (2)$$

Therefore, the evolution from the dispersive band to the flat band (e.g., the TE2 band from Figure 1(c) to (d)) can be achieved by tuning the layer misalignment.

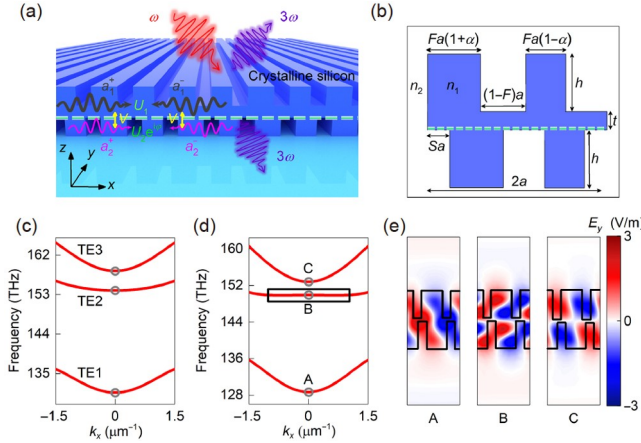The high Q factor of the three modes leads to high local

Figure 1 (Color online) (a) Schematic of the asymmetric "*fishbone*" metagratings. Photons of a fundamental pump at ω are converted to photons at 3ω via THG. (b) Elementary cell of "*fishbone*" metagratings, divided by an imaginary dotted line. The structure is in the background of air with period $2a$, thickness of the lower grating h, dimensionless layer misalignment S, perturbation factor α, filling factor F, and thickness of the central waveguide t. (c) Calculated three TE dispersive bands along the k_x axis. (d) Calculated three TE bands along the k_x axis with the TE2 band flat in the black box. (e) Eigenfield distributions (y component) E_y of three Γ points (A-C) in (d). The structural parameters of the flat-band metagratings are $2a = 1.05$ μm, $h = 0.61$ μm, $S = 0.23$, $\alpha = 0.081$, $F = 0.595$, and $t = 52.5$ nm.

field enhancements, strengthening nonlinear light-matter interactions inside the meta-atoms. Specifically, the TE2 band is engineered into a flat band since its electric field is more localized in the dielectric media compared with other modes (Figure 1(e)), in favor of higher nonlinear conversion efficiency. However, the three modes are all waveguide modes with an infinite quality (Q) factor below the light cone and cannot be excited with the perturbation factor $\alpha = 0$. To transform the bound modes into quasi-BICs through band folding, we introduce a double-period perturbation. The perturbative factor $\alpha \ll 1$ offers weak couplings to the radiative waves (the scaling law of Q for quasi-BICs in this system satisfies $Q \propto \alpha^{-2}$ [18]) and a small perturbation of the Hamiltonian. In the simulation of the quasi-BIC flat band, the metagrating is composed of crystalline silicon (c-Si, $\chi_{Si}^{(3)} = 2.79 \times 10^{-18}\,\mathrm{m}^2 \cdot \mathrm{V}^{-2}$), and the relative permittivity of c-Si is modeled by an N-pole Lorentz function in the eigenvalue solver (COMSOL) to address the dispersion of the optical constant [36]. The wavelength range of the dispersion of the permittivity in our simulations is from 317 to 3000 nm [36], which contains the fundamental wavelength and third harmonic wavelength.

3   Results and discussions

We excite several typical resonances on this flat band and investigate their corresponding nonlinear generations within

wide operating angles. The total THG emission can be estimated by the nonlinear scattering theory [37,38]. The fundamental electric field distributions $|E^{\mathrm{FF}}|$ with incident angles of 6º, 13º, and 20º at resonant frequencies are shown in Figure 2(a)-(c), and the harmonic counterparts E_y^{TH} are shown in Figure 2(d)-(f). Both the fundamental field distributions and amplitudes among different angles are analogous, as shown in Figure 2(a)-(c), which suggests the weak angular dispersion of linear processes. In remarkable contrast, the nonlinear near-field amplitude of $\theta = 13$º is higher than that of 6º and 20º with comparative field distributions (phases), as shown in Figure 2(d)-(f).

To clarify the distinct dispersion behavior between linear and nonlinear processes, we adopted the multipolar analysis in linear and nonlinear regimes. The scattering power can be expressed in terms of multipolar modes as refs. [39,40], in which the predominant modes of electric dipole (ED) and magnetic dipole (MD) are shown in Figure 2(g) and (h). For the linear process, both the ED and MD modes distinctly respond at the resonant frequency. The MD mode is excited with a larger intensity than the ED mode in the whole linear process, and its corresponding resonant intensity alters little at four angles, as shown in Figure 2(g). This small variation of the MD modes corresponds to the weak angular dispersion of the output signals in Figure 2(a)-(c). However, for the nonlinear process, the MD mode is mainly excited with the ED mode almost zero, as shown in Figure 2(h). This contrast between the linear and nonlinear resonance is mainly affected by the MD mode. In nonlinear processes, the MD resonant intensity of $\theta = 15$º is the highest, as shown in Figure 2(h), demonstrating that weak angular dispersion in linear processes cannot be achieved in the nonlinear regime according to their different multipolar intensities, as shown in Figure 2(g) and (h). Furthermore, the nonlinear MD resonant intensities of $\theta = 6$º, 13º, 20º correspond to their nonlinear field enhancements (Figure 2(d)-(f)), showing the maximum at $\theta = 13$º.

To analyze the effects of different modes in the whole process of nonparaxial flat-band-based nonlinear generation, we introduce the quasinormal modes (QNM) method [41,42], which expands the excited field by eigenstate modes of nanoresonators [43,44]. Without loss of generality, we apply the QNM theory to the case of $\theta = 15$º (strongest nonlinear signal), as shown in Figure 3(a). Third-harmonic generation (THG) can be described via two coherent processes. First, the resonator is excited by an external driving field $[E_b\ (k, r, \omega), H_b\ (k, r, \omega)]$ to generate a total field distribution $[E_t\ (k, r, \omega), H_t\ (k, r, \omega)]$ at the fundamental frequency (FF) ω. Second, the total FF field generates a local nonlinear polarization $P^{(3)}\ (k_x, y)$, acting as the source for the THG. We consider several QNMs that cover the spectral range from ω to 3ω. The normalized electric and magnetic

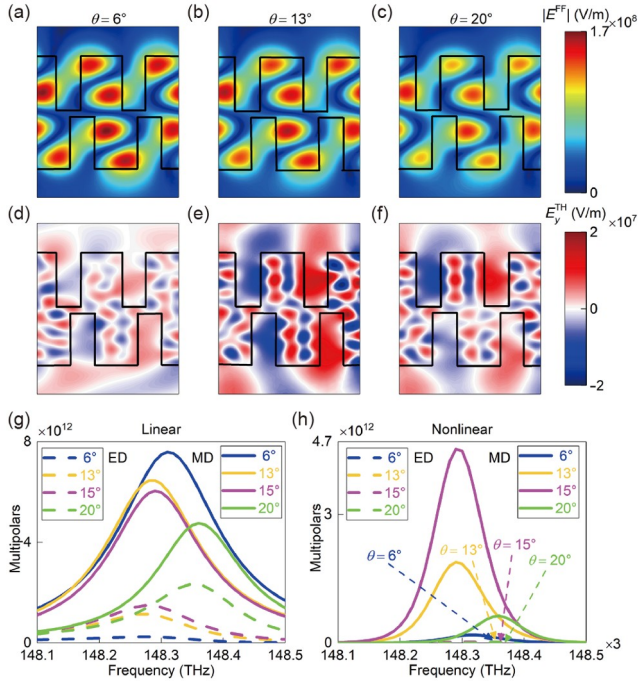**Figure 2** (Color online) (a)-(c) Fundamental electric field distributions $|E^{FF}|$ at resonant frequencies under incident angles of $\theta = 6º$, $13º$, and $20º$ (left to right). (d)-(f) Harmonic electric field distributions (y component) E_y^{TH} at resonant frequencies under incident angles of $\theta = 6º$, $13º$, and $20º$ (left to right). (g), (h) Multipolar decompositions of the scattering power in terms of ED (dotted lines) and MD (solid lines) under $\theta = 6º$, $13º$, $15º$, and $20º$ in linear and nonlinear processes, respectively. The metagrating is excited by a TE plane wave with intensity $I_0 = 0.047$ GW/cm^2.

distributions of the m-th QNM are denoted by $\left[\widetilde{E}_m(r), \widetilde{H}_m(r)\right]$. Importantly, the QNM fields must be normalized such that $\int\left[\widetilde{E}_m \cdot (\partial\omega\varepsilon / \partial\omega)\widetilde{E}_m - \widetilde{H}_m \cdot (\partial\omega\mu / \partial\omega)\widetilde{H}_m\right]dr = 1$ [42]. The total field inside the resonator at w can be reconstructed as:

$$E_t(k_x, y, \omega) = \sum_{m=1}^{M_1} \alpha_m^{(1)}(k_x, \omega) \frac{\varepsilon(k_x, \widetilde{\omega}_m) - \varepsilon_\infty}{\varepsilon(k_x, \omega) - \varepsilon_\infty}\widetilde{E}_m(k_x, y), \qquad (3)$$

where $\alpha_m^{(1)}(k_x, \omega)$ represents the excitation coefficient of the m-th QNM at FF, with complex frequency $\widetilde{\omega}_m$, $\left[\widetilde{E}_m(r), \widetilde{H}_m(r)\right]$ is the normalized electric and magnetic distributions of the m-th QNM and ε_∞ is the permittivity $\varepsilon(k_x, \omega \to \infty)$. For a resonator with N-pole Lorentz permittivity, a classical and well-documented expression is

$$\alpha_m^{(1)}(k_x, \omega) = \int_V \left\{ \frac{[\varepsilon(\widetilde{\omega}_m) - \varepsilon_b]\widetilde{\omega}_m(k_x)}{\widetilde{\omega}_m(k_x) - \omega(k_x)} + (\varepsilon_b - \varepsilon_\infty) \right\}$$
$$\times \widetilde{E}_m(k_x, y) \cdot E_b(k_x, y, \omega)dr. \qquad (4)$$

Here, $\varepsilon_b(k_x)$ is the background permittivity. The integral is performed on the volume V, which defines the resonator in the scattering field formulation.

The total field of eq. (4) generates a nonlinear polarization

in the grating:

$$P^{(3)}(k_x, y) = 3\varepsilon_0\chi^{(3)}\left[E_t(k_x, y, \omega)\right]^3. \qquad (5)$$

The total field $E_t(k_x, y, 3\omega)$ at 3ω can also be expanded by the QNMs:

$$E_t(k_x, y, 3\omega) = \sum_{l=1}^{M_2} \alpha_l^{(3)}(k_x, 3\omega)\widetilde{E}_l(k_x, y), \qquad (6)$$

where the m-th QNM excitation coefficient at third harmonic (TH) frequency can be expressed as:

$$\alpha_l^{(3)}(k_x, 3\omega) = \frac{-3\omega(k)k_x}{\widetilde{\omega}_l(k_x) - 3\omega(k_x)}\int_V P^{(3)}(k_x, y, 3\omega) \cdot \widetilde{E}_l(k_x, y)dr. \qquad (7)$$

We show the frequency positions in the complex wavelength plane (λ_m) of the typical QNMs (FF1-FF3 and TH1-TH6) by calculating the excitation coefficients (eqs. (4) and (7)) of QNMs in the vicinity of fundamental and third harmonic frequencies, as shown in Figure 3(c). Their corresponding field distributions are shown in Figure 3(d). Based on eqs. (3) and (6), every QNM is a basis of the actual excited field in the Hilbert space. The actual off-axis THG excited field (Figure 3(b)) can be obtained by a linear combination of typical TH QNMs in Figure 3(d). Generally, all situations with an excitation source can be analyzed by this QNM decomposition, focusing on correlative overlap integrals of the excitation field and the QNM field, as described in eqs. (4) and (7).

To further demonstrate the flat-band-based high nonlinear conversion efficiency, we set the incident plane-wave angles as 0º, 5º, 10º, 15º, and 20º, within the operating angular range of the flat band. Figure 4(a) and (b) show the corresponding five THG conversion efficiencies of the flat and dispersive-band-based metagratings, respectively, where $\eta_{THG} = P_{3\omega}/P_\omega$ ($P_\omega = 2aI_0\cos\theta$) contains all diffraction components, and two THG conversion efficiencies of 0º are both 0.03. All conversion efficiencies are close to 0.03 except for the case of 15º reaching 0.1, as shown in Figure 4(a). In contrast, the THG conversion efficiency decreases rapidly to 8.9×10^{-5} as the incident angle θ increases in Figure 4(b). Meanwhile, the resonant frequencies of different incident angles are always approximately 148.3 THz for flat-band excitation; nevertheless, the resonant frequency increases as the incident angle θ increases for the dispersive band, as shown in Figure 4(a) and (b). We further calculated the total THG conversion efficiencies of these two metagratings with the simultaneous incidence of five plane waves, as depicted in the inset of Figure 4(c). The total nonlinear conversion efficiency assisted by the flat band is an order of magnitude higher than that of the dispersive band, as shown in Figure 4(c), which is robust with parametric deviation of the structures such as wider/narrower comb widths and more/less layer misalignment, which correspond to the common fabrication accuracy
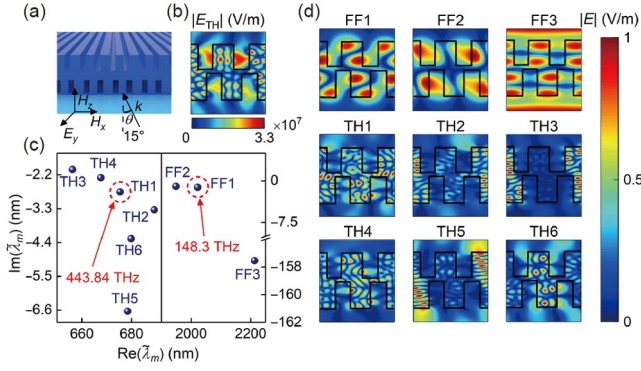
Figure 3 (Color online) (a) Set of QNMs excited by the plane wave with the incident angle $\theta = 15°$ and the intensity $I_0 = 0.047$ GW/cm^2. (b) The harmonic field distribution $|E_{TH}|$ of $\theta = 15°$ at the resonant frequency. (c) Eigenfrequency positions of QNMs near the TH and FF in the wavelength-space complex plane. (d) Corresponding eigenfield distributions $|E|$ of (c). Every field in (d) is normalized by its maximum amplitude.

of fabrication of 10 and 20 nm (Supporting Material III), demonstrating the flat-band-based constructive superposition of the nonlinear conversion among different plane-wave components. Although the THG conversion efficiency of 15° incidence is much higher than that of the other angles, the higher total THG conversion efficiency of the flat band in Figure 4(c) results from the coherent superposition of the nonlinear generation at every incident angle. The nonlinear conversion efficiencies with and without 15° incidence are comparable, as shown in Figure 4(d).

The nonlinear conversion efficiency can be significantly enhanced since not only the good spectral overlap guaranteed by the total shift in the resonant wavelength smaller than the full width at half maximum (FWHM) of the resonance but also the constructive superposition guaranteed by comparative THG field distributions (phases) (Supporting Material IV). We select the spectrum of 15° with the highest THG conversion efficiency in Figure 4(a) and estimate its Q factor through FWHM [45]. The good spectral overlap is satisfied when the pumped incident angles of the THG conversion efficiency spectra range from −20° to 20° (fundamental resonant frequencies are in the FWHM of 15°, $Q = 1100.1$), as shown in the yellow region in Figure 4(e). The total THG efficiency can be improved by this good spectral overlap of different incident components in addition to the constructive superposition of comparable THG phases among different plane-wave components (Supporting Material IV). In contrast, good spectral overlap may only occur among the THG conversion efficiencies from the resonant frequency of $\theta = -5°$ to the resonant frequency of $\theta = 5°$ ($Q = 983.59$), as shown in the orange region in Figure 4(f), regardless of the pumped incident angle for the dispersive-band counterpart. The constructive superposition of comparable THG phases of the dispersive band from −20° to 20° is ineffective (Supporting Material IV). Thus, the total
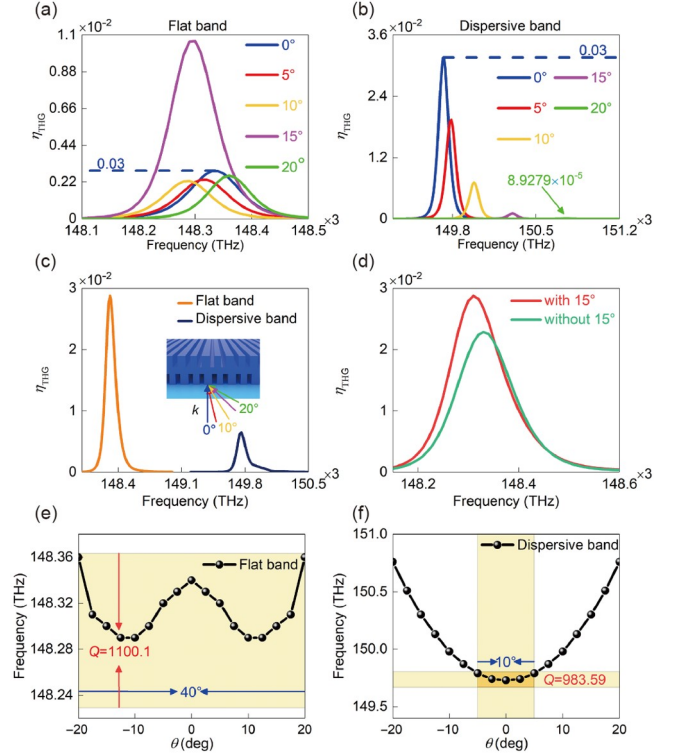

Figure 4 (Color online) (a), (b) The THG conversion efficiency (η_{THG}) spectra of the flat and dispersive-band metagratings as a function of the harmonic frequency under different incident angles of 0°, 5°, 10°, 15°, and 20°. The excitation intensity is $I_0 = 0.047$ GW/cm^2 for both the flat-band and dispersive-band metagratings. The η_{THG} of $\theta = 0°$ in (a) and (b) are comparable (0.03). (c) Total η_{THG} spectra of the flat and dispersive-band metagratings as a function of the harmonic frequency with the simultaneous incidence of five plane waves, as depicted in the inset of (c). (d) Total η_{THG} spectra of flat-band-based nonlinear generation with and without 15° incidence. (e) The operating angular range of 40° guarantees good spectral overlap (yellow regime) for the flat-band metagratings. (f) The operating angular range of 10° guarantees good spectral overlap (orange regime) for dispersive-band metagratings. The structural parameters of the dispersive bands are $2a = 1.05$ μm, $h = 0.63$ μm, $S = 0.3$, $\alpha = 0.1$, $F = 0.57$, and $t = 52.5$ nm.

nonlinear conversion efficiency assisted by the dispersive band is lower than that of the flat band.

The flat-band metagrating can be well applied to wavefront control in practical applications, with output signal intensities varying with different diffraction orders. For example, more diffraction orders of η_{THG} (R) (THG signal of the reflection port) are generated as the incident angle θ increases at the fundamental frequency of 148.3 THz, as shown in Figure 5(a). This wavefront control can also be demonstrated by calculating the difference in η_{THG} (R) [$\Delta\eta_{THG}$ (R)] at various incident angles and harmonic resonant frequencies, as shown in Figure 5(b). We further observe the THG far-field polarization distributions of two points ($\theta = 7.5°$ and 15°) near the maximum value of $\Delta\eta_{THG}$ (R) in Figure 5(b) and mark them with five-pointed stars at the same fundamental resonant frequency of 148.3 THz. The diffraction orders of −1 and 1 dominate at $\theta = 7.5°$ and $\theta = 15°$, respectively, as shown in Figure 5(c) and (d). The insets

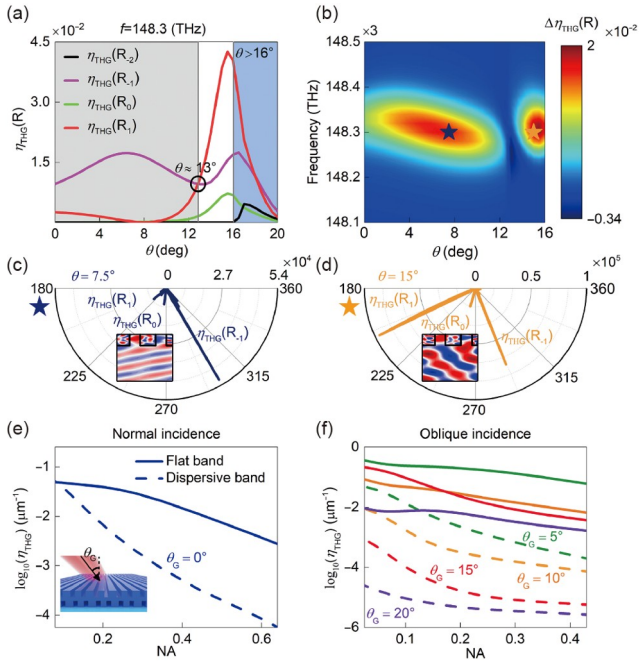**Figure 5** (Color online) (a) The η_{THG} (R) (THG of the reflective component) spectra of different diffraction orders as a function of the incident angle θ at the fundamental resonant frequency of 148.3 THz. (b) The difference in η_{THG} (R) [$\Delta\eta_{THG}$ (R)] for fundamental frequencies ranging from 148.1 to 148.5 THz as a function of the incident angle θ. ($\Delta\eta_{THG}$ (R) = η_{THG} (R$_{-1}$) − η_{THG} (R$_0$) − η_{THG} (R$_1$) and $\Delta\eta_{THG}$ (R) = η_{THG} (R$_1$) − η_{THG} (R$_0$) − η_{THG} (R$_{-1}$) for $\theta \leq 13°$ and $\theta > 13°$, respectively). Two points ($\theta = 7.5°$ and 15°) are marked with five-pointed stars at the same fundamental resonant frequency of 148.3 THz. (c), (d) THG far-field polarization distributions of the two points in (b). The number of unit cells $N = 40$, and the excitation intensity $I_0 = 0.047$ GW/cm^2. The insets show the electric field distributions of the periodic structure. (e), (f), The total η_{THG} (normalized by the total thickness of the metagratings) spectra of the flat and dispersive-band metagratings as a function of NA under the Gaussian beam being incident at $\theta_G = 0°$ (e) and $\theta_G = 5°$, 10°, 15°, 20° (f). The axial component of the Gaussian beam is $I_G = 0.1$ GW/cm^2.

are their corresponding electric field distributions of the periodic structure, obviously showing the plane waves of the THG with different reflected angles θ_r, where θ_r can be calculated by the grating equation of $2a(\sin\theta_r + \sin\theta) = q\lambda$ (q is the diffraction order, and λ is the incident wavelength).

In particular, we use the Gaussian beam to verify the high total THG conversion efficiency of flat-band-based nonlinear generation again, considering its high use in practical applications. The Gaussian beam is incident at $\theta_G = 0°$, 5°, 10°, 15°, and 20° for both quasi-BIC flat-band and dispersive-band metagratings. The THG conversion efficiency of the flat-band metagratings is higher than that of the dispersive counterpart; in particular, $\log_{10}(\eta_{THG})$ reaches approximately two orders of magnitude higher at a large numerical-aperture (NA) of approximately 0.65 for normal incidence, as shown in Figure 5(e). This contrast between the flat and dispersive-band metagratings will also exist for the oblique incidence in Figure 5(f) with NA ranging from 0 to 0.43 (Supporting Material II).

4 Conclusions

In conclusion, based on the intralayer and interlayer diffractive couplings of the "*fishbone*" metagrating with the mirror symmetry broken, we realized a quasi-BIC flat band systematically investigated the corresponding off-axis nonlinear generation. We clarified that the angular dispersion of the output signal in the linear regime cannot directly correspond to that of the nonlinear regime under plane waves being incident at different angles. We elucidated the mechanism of this off-axis flat-band-based nonlinear generation through different mode decompositions. The flat-band-based nonlinear conversion efficiency is higher than the dispersive counterpart. This is robust under normal and oblique large-NA incidence, which results from the good spectral overlap of different plane-wave components and constructive superposition of corresponding THG phases. This robustness can enable predesigned structural beams consisting of different wide-angle components to effectively improve the nonlinear conversion efficiency. This work paves the way for not only deeper investigations of the angular dispersion problem in the nonlinear regime but also applications involving different wide-angle components, such as nonlinear multichannel optical manipulation, nonlinear optical communication, and large field-of-view nonlinear imaging.

Conflict of interest   The authors declare that they have no conflict of interest

Supporting Information

The supporting information is available online at http://phys.scichina.com and https://link.springer.com. The supporting materials are published as submitted, without typesetting or editing. The responsibility for scientific accuracy and content remains entirely with the authors.

1 K. Tamasaku, E. Shigemasa, Y. Inubushi, I. Inoue, T. Osaka, T. Katayama, M. Yabashi, A. Koide, T. Yokoyama, and T. Ishikawa, Phys. Rev. Lett. **121**, 083901 (2018).

2 T. C. Wei, S. Mokkapati, T. Y. Li, C. H. Lin, G. R. Lin, C. Jagadish, and J. H. He, Adv. Funct. Mater. **28**, 1707175 (2018).

3 Y. Dai, Y. Wang, S. Das, S. Li, H. Xue, A. Mohsen, and Z. Sun, Nano Lett. **21**, 6321 (2021).

4 F. A. Sabattoli, H. E Dirani, L. Youssef, F. Garrisi, D. Grassani, L. Zatti, C. Petit-Etienne, E. Pargon, J. E. Sipe, M. Liscidini, C. Sciancalepore, D. Bajoni, and M. Galli, Phys. Rev. Lett. **127**, 033901 (2021).

5 Z. Hao, W. Liu, Z. Li, Z. Li, G. Geng, Y. Wang, H. Cheng, H. Ahmed, X. Chen, J. Li, J. Tian, and S. Chen, Laser Photon. Rev. **15**, 2100207 (2021).

6 A. Fedotova, M. Younesi, J. Sautter, A. Vaskin, F. J. F. Löchner, M. Steinert, R. Geiss, T. Pertsch, I. Staude, and F. Setzpfandt, Nano Lett. **20**, 8608 (2020).

7   G. Barbet, B. Qiang, Y. Jin, T. Wu, P. Genevet, Q. Wang, and Y. Luo, Adv. Opt. Mater. **11**, 2202786 (2023).

8   V. Giovannetti, L. Maccone, J. H. Shapiro, and F. N. C. Wong, Phys. Rev. A **66**, 043813 (2002).

9   M. T. Turnbull, P. G. Petrov, C. S. Embrey, A. M. Marino, and V. Boyer, Phys. Rev. A **88**, 033845 (2013).

10   Z. Li, W. Liu, D. Ma, S. Yu, H. Cheng, D. Y. Choi, J. G. Tian, and S. Chen, Phys. Rev. Appl. **17**, 024008 (2022).

11   W. Liu, Z. Li, M. A. Ansari, H. Cheng, J. Tian, X. Chen, and S. Chen, Adv. Mater. **35**, 2208884 (2023).

12   D. N. Neshev, and A. E. Miroshnichenko, Nat. Photon. **17**, 26 (2023).

13   T. Gu, H. J. Kim, C. R. Baleine, and J. Hu, Nat. Photon. **17**, 48 (2023).

14   Y. Zhang, Z. Li, W. Liu, Z. Li, H. Cheng, J. Tian, and S. Chen, Opt. Lett. **46**, 3528 (2021).

15   L. Ni, Z. Wang, C. Peng, and Z. Li, Phys. Rev. B **94**, 245148 (2016).

16   R. Chai, Q. Liu, W. Liu, Z. Li, H. Cheng, J. Tian, and S. Chen, ACS Photon. **10**, 2031 (2023).

17   R. Chai, W. Liu, Z. Li, H. Cheng, J. Tian, and S. Chen, Phys. Rev. B **104**, 075149 (2021).

18   K. Koshelev, S. Lepeshov, M. Liu, A. Bogdanov, and Y. Kivshar, Phys. Rev. Lett. **121**, 193903 (2018).

19   S. Xiao, M. Qin, J. Duan, F. Wu, and T. Liu, Phys. Rev. B **105**, 195440 (2022).

20   Z. Zheng, L. Xu, L. Huang, D. Smirnova, P. Hong, C. Ying, and M. Rahmani, Phys. Rev. B **106**, 125411 (2022).

21   C. Huang, C. Zhang, S. Xiao, Y. Wang, Y. Fan, Y. Liu, N. Zhang, G. Qu, H. Ji, J. Han, L. Ge, Y. Kivshar, and Q. Song, Science **367**, 1018 (2020).

22   M. S. Hwang, H. C. Lee, K. H. Kim, K. Y. Jeong, S. H. Kwon, K. Koshelev, Y. Kivshar, and H. G. Park, Nat. Commun. **12**, 4135 (2021).

23   X. Zhang, Y. Liu, J. Han, Y. Kivshar, and Q. Song, Science **377**, 1215 (2022).

24   R. Camacho-Morales, L. Xu, H. Zhang, S. T. Ha, L. Krivitsky, A. I. Kuznetsov, M. Rahmani, and D. Neshev, Nano Lett. **22**, 6141 (2022).

25   G. Grinblat, ACS Photon. **8**, 3406 (2021).

26   T. Liu, M. Qin, F. Wu, and S. Xiao, Phys. Rev. B **107**, 075441 (2023).

27   Y. Liang, H. Lin, S. Lin, J. Wu, W. Li, F. Meng, Y. Yang, X. Huang, B. Jia, and Y. Kivshar, Nano Lett. **21**, 8917 (2021).

28   L. Huang, W. Zhang, and X. Zhang, Phys. Rev. Lett. **128**, 253901 (2022).

29   H. S . Nguyen, F. Dubois, T. Deschamps, S. Cueff, A. Pardon, J. L. Leclercq, C. Seassal, X. Letartre, and P. Viktorovitch, Phys. Rev. Lett. **120**, 066102 (2018).

30   Y. Yang, C. Roques-Carmes, S. E. Kooi, H. Tang, J. Beroz, E. Mazur, I. Kaminer, J. D. Joannopoulos, and M. Soljačić, Nature **613**, 42 (2023).

31   S. M. Kamali, E. Arbabi, A. Arbabi, Y. Horie, M. Faraji-Dana, and A. Faraon, Phys. Rev. X **7**, 041056 (2017).

32   K. Shastri, and F. Monticone, Nat. Photon. **17**, 36 (2023).

33   C. Zhou, W. B. Lee, C. S. Park, S. Gao, D. Y. Choi, and S. S. Lee, Adv. Opt. Mater. **8**, 2000645 (2020).

34   S. G. Lee, S. H. Kim, and C. S. Kee, Phys. Rev. Lett. **126**, 013601 (2021).

35   Y. Yang, C. Peng, Y. Liang, Z. Li, and S. Noda, Phys. Rev. Lett. **113**, 037401 (2014).

36   M. Garcia-Vergara, G. Demésy, and F. Zolla, Opt. Lett. **42**, 1145 (2017).

37   K. O'Brien, H. Suchowski, J. Rho, A. Salandrino, B. Kante, X. Yin, and X. Zhang, Nat. Mater **14**, 379 (2015).

38   M. S. Nezami, D. Yoo, G. Hajisalem, S. H. Oh, and R. Gordon, ACS Photon. **3**, 1461 (2016).

39   S. Kruk, and Y. Kivshar, ACS Photon. **4**, 2638 (2017).

40   Z. Huang, K. Luo, Z. Feng, Z. Zhang, Y. Li, W. Qiu, H. Guan, Y. Xu, X. Li, and H. Lu, Sci. China-Phys. Mech. Astron. **66**, 284211 (2023).

41   R. Colom, F. Binkowski, F. Betz, Y. Kivshar, and S. Burger, Phys. Rev. Res. **4**, 023189 (2022).

42   C. Gigli, T. Wu, G. Marino, A. Borne, G. Leo, and P. Lalanne, ACS Photon. **7**, 1197 (2020).

43   P. Lalanne, W. Yan, K. Vynck, C. Sauvan, and J. P. Hugonin, Laser Photon. Rev. **12**, 1700113 (2018).

44   Q. Zhou, P. Zhang, and X. W. Chen, Phys. Rev. Lett. **127**, 267401 (2021).

45   Q. Zhang, M. Lou, X. Li, J. L. Reno, W. Pan, J. D. Watson, M. J. Manfra, and J. Kono, Nat. Phys. **12**, 1005 (2016).